PERGAMON

International Journal of Heat and Mass Transfer 45 (2002) 1849–1863

International Journal of HEAT and MASS TRANSFER

www.elsevier.com/locate/ijhmt

Computational modeling for honeycomb-stator gas annular seal

G. Chochua [a], W. Shyy [a,*], J. Moore [b]

[a] *Department of Aerospace Engineering, Mechanics and Engineering Science, University of Florida, 231 Aerospace Building, P.O. Box 116250, Gainesville, FL 32611-6250, USA*

[b] *Rotordynamics Group, Dresser-Rand Co., Olean, NY 14760, USA*

Received 10 May 2001; received in revised form 23 August 2001

Abstract

Gas annular seals are commonly adopted for leakage control in turbomachinery applications. Honeycomb seals are attractive from the viewpoints of leakage control as well as rotordynamic stability. To improve our understanding of thermo-fluid-physics in such seals, a computational capability is developed for low Mach number, compressible, turbulent flows. The emphases of the present study include (i) development of an original numerical scheme with periodic boundary conditions for flows around repeated geometries, (ii) evaluation of a low Reynolds number version of the k–ε turbulence model suitable for the operating conditions of honeycomb seals, and (iii) 3-D computations to assess the implications of the numerical predictions for practical configurations including velocity, pressure, temperature characteristics and loss mechanisms.

1. Introduction

Gas annular seals are commonly adopted for turbomachinery applications to reduce leakage, thus improving efficiency. Widely used labyrinth seals combine good leakage performance and low cost. However, operating at high pressures and tight clearances, they may develop significant force imbalance to cause rotordynamic instabilities. Honeycomb seals were first applied to improve rotordynamic performance in High Pressure Oxygen Turbopump (HPOTP) of Space Shuttle main engine [1] in 1989. A schematic of honeycomb seal between a stator and smooth rotor geometry is shown in Fig. 1. Honeycomb seals provide resistance to flow in axial as well as circumferential directions, and are found to reduce the tendency of rotordynamic instabilities. Childs et al. [2] have conducted extensive experimental investigations for honeycomb seals, and show that the best sealing and rotordynamic performance for such seals, with swirling incoming flows and followed by labyrinth seals, is achieved for seals that longer than around 50 mm. For shorter seals, say, 25 mm in length, the rotordynamic stability advantage is diminished [3].

Traditionally, the analytical study of flow in seals is based on the bulk flow theory of Hirs [4]. This theory is an extension of a rough pipe flow to accommodate the annular geometry. However, flows in honeycomb seals behave quite differently compared to those in rough pipes. To gain more understanding of the thermo-fluid-physics, Ha and Childs [5,6] have investigated flows between two parallel honeycomb plates. They demonstrate that the friction factor is sensitive to changes in cell geometry, making it necessary to adjust empirical coefficients of the theories for the individual honeycomb geometry. Needless to say, such case-by-case adjustment precludes the development of any predictive capabilities. In addition, experimental studies also show a strong dependence of the friction factor from the Reynolds number in certain situations, including dramatic drop and rise of the friction factor [7]. Full Navier–Stokes solutions for such flow problems are challenging due to the complex geometry and physics involved. Hendricks et al. [8] have reported their computational work for flows between two flat honeycomb plates, based on the case studies carried out experimentally by Ha and Childs

* Corresponding author. Tel.: +1-352-392-0961; fax: +1-352-392-7303.

E-mail address: wss@aero.ufl.edu (W. Shyy).

0017-9310/02/$ - see front matter
PII: S0017-9310(01)00280-0

Nomenclature

A	area
A_w	area of the effective plate surfaces
C_μ, $C_{\varepsilon 1}$, $C_{\varepsilon 2}$	turbulence closure coefficients
D, E	near wall damping functions, used in low *Re* turbulence models
H	stagnation enthalpy per unit mass
L	length
M	Mach number
Pr_L	laminar Prandtl number
Pr_t	turbulent Prandtl number
R	gas constant
R_T	turbulent Reynolds number
Re	Reynolds number
T	temperature
T_i	turbulent intensity
T_t	total temperature
U	mean (bulk) flow velocity
X, Y, Z	coordinates
f	friction factor
f_p	pressure component of the friction factor
f_τ	shear stress component of the friction factor
d	seal diameter
h_e	enthalpy per unit mass
h	clearance
k	kinetic energy of turbulence per unit mass
l	turbulent length scale
$\dot{m}$	mass flow rate
n_3	direction cosine between a surface normal and Z direction
p	pressure
t	turbulent time scale
t_3	direction cosine between wall shear stress vector and Z direction
u	Cartesian velocity component
x	Cartesian coordinate
y	distance from the wall
y^+	non-dimensional distance from the wall in turbulent flows
$\hat{y}$	distance from the wall normalized by clearance

Greek symbols

β	mesh stretching parameter
δ	boundary layer thickness
δ_{ij}	Dirac delta function
ε	turbulent kinetic energy dissipation rate
$\hat{\varepsilon}$	effective turbulent kinetic energy dissipation rate
μ	molecular viscosity
μ_t	eddy viscosity
v	kinematic viscosity ($=\mu/\rho$)
ρ	density
σ_k, σ_ε	turbulence closure coefficients
τ_{wall}	wall shear stress

Subscripts

i, j, k, l	cyclical indices or indices along x, y, z direction
i	index of structured grid
in	denotes inlet
mid	denotes middle of computational domain in flow direction

Superscripts

$'$	denotes fluctuation in turbulent flow, conventionally averaged variables
$''$	denotes fluctuation in turbulent flow, mass-averaged variables

Overbars

–	denotes conventionally averaged quantity
$\sim$	denotes mass-averaged variables

[5]. However, little quantitative information is provided to allow detailed evaluation of their efforts. In the present study, we develop and refine computational techniques from both numerical and modeling viewpoints, with the goal of evaluating computational fluid dynamics (CFD) capabilities with the aid of experimental information. Specifically, the emphases of the present study include (i) development of an original numerical scheme with periodic boundary conditions for compressible, turbulent flows around geometries with repeated patterns, (ii) evaluation of a low Reynolds number version of the k–ε turbulence model suitable for the operating conditions of honeycomb seals, and (iii) detailed 3-D computations to assess the implications of the numerical predictions for practical configurations. In the following, we will first present the governing equations, followed by the development and assessment of the numerical and modeling issues, and then present several case studies based on the experiments with direct relevancy to honeycomb seal applications.

2. Numerical techniques

3-D compressible Navier–Stokes equations are solved in body-fitted coordinates, based on the finite volume formulation. Second-order schemes are adopted, with the upwind arrangement for convection, and cen-

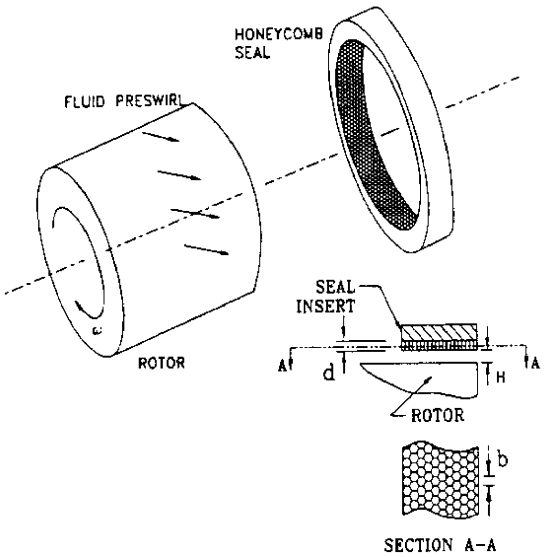

Fig. 1. Schematic honeycomb seal geometry, adopted from Ha and Childs [5].

tral difference for other terms [9,10]. The solution procedure employs a unified pressure-based algorithm [10,11] in structured multiblock grid [12]. The turbulence closure is modeled using the k–ε model [13] accounting for the low Reynolds number effect, proposed by Chien [14].

2.1. Governing equations

The Favre-averaged Navier–Stokes equations [11] for compressible, turbulent flows are adopted in the present study. The individual equations are presented below.

Continuity equation:

$$\frac{\partial \overline{\rho}}{\partial t}+\frac{\partial}{\partial x_j}\left(\overline{\rho}\tilde{u}_j\right)=0. \tag{1}$$

Momentum equation:

$$\frac{\partial}{\partial t}\left(\overline{\rho}\tilde{u}_i\right)+\frac{\partial}{\partial x_j}\left(\overline{\rho}\tilde{u}_i\tilde{u}_j\right) =-\frac{\partial \overline{p}}{\partial x_i}+\frac{\partial}{\partial x_j}\left[(\mu+\mu_{\mathrm{t}})\left(\frac{\partial \tilde{u}_i}{\partial x_j}+\frac{\partial \tilde{u}_j}{\partial x_i}-\frac{2}{3}\frac{\partial \tilde{u}_l}{\partial x_l}\delta_{ij}\right)\right]. \tag{2}$$

Stagnation enthalpy ($\tilde{H}=\tilde{h}_{\mathrm{e}}+\frac{1}{2}\tilde{u}_i\tilde{u}_i+k$) *equation*:

$$\frac{\partial}{\partial t}\left(\overline{\rho}\tilde{H}-\overline{p}\right)+\frac{\partial}{\partial x_j}\left(\overline{\rho}\tilde{u}_j\tilde{H}\right) =\frac{\partial}{\partial x_j}\left[\left(\frac{\mu}{Pr_{\mathrm{L}}}+\frac{\mu_{\mathrm{t}}}{Pr_{\mathrm{t}}}\right)\frac{\partial \tilde{h}_{\mathrm{e}}}{\partial x_j}\right]+\frac{\partial}{\partial x_j}\left[\left(\mu+\frac{\mu_{\mathrm{t}}}{\sigma_k}\right)\frac{\partial k}{\partial x_j}\right] +\frac{\partial}{\partial x_j}\left[\tilde{u}_i\left\{(\mu+\mu_{\mathrm{t}})\left(\frac{\partial \tilde{u}_i}{\partial x_j}+\frac{\partial \tilde{u}_j}{\partial x_i}-\frac{2}{3}\frac{\partial \tilde{u}_l}{\partial x_l}\delta_{ij}\right)\right\}\right]. \tag{3}$$

Equation of state:

$$\overline{p}=\overline{\rho}R\tilde{T}. \tag{4}$$

The Reynolds stresses are approximated using the Boussinesq eddy viscosity approximation. The governing equations are discretized and flux constructed employing the body-fitted curvilinear coordinates.

2.2. Turbulence model

The original k–ε turbulence model [13] with low Reynolds number modifications, proposed by Chien [14], is applied to represent the Reynolds stresses

$$-\overline{\rho u_i'' u_j''}=\mu_{\mathrm{t}}\left(\frac{\partial \tilde{u}_i}{\partial x_j}+\frac{\partial \tilde{u}_j}{\partial x_i}\right)-\frac{2}{3}\mu_{\mathrm{t}}\frac{\partial \tilde{u}_l}{\partial x_l}\delta_{ij}-\frac{2}{3}\overline{\rho}k\delta_{ij}. \tag{5}$$

The turbulent time and length scales are provided by turbulent kinetic energy, k, and effective eddy dissipation rate, $\hat{\varepsilon}$

$$\mu_{\mathrm{t}}=\overline{\rho}\frac{l^2}{t}=\overline{\rho}C_{\mu}\frac{k^2}{\hat{\varepsilon}}. \tag{6}$$

The two transport equations have the following forms:

$$\frac{\partial}{\partial t}\overline{\rho}k+\frac{\partial}{\partial x_i}(\overline{\rho}\tilde{u}_i k)=\frac{\partial}{\partial x_i}\left[\left(\mu+\frac{\mu_{\mathrm{t}}}{\sigma_k}\right)\frac{\partial k}{\partial x_i}\right]+\Pi-\overline{\rho}\varepsilon, \tag{7}$$

$$\frac{\partial}{\partial t}\overline{\rho}\hat{\varepsilon}+\frac{\partial}{\partial x_i}(\overline{\rho}\tilde{u}_i\hat{\varepsilon})=\frac{\partial}{\partial x_i}\left[\left(\mu+\frac{\mu_{\mathrm{t}}}{\sigma_{\varepsilon}}\right)\frac{\partial \hat{\varepsilon}}{\partial x_i}\right]+\frac{C_{\varepsilon 1}\hat{\varepsilon}\Pi}{k} -C_{\varepsilon 2}\overline{\rho}\frac{\hat{\varepsilon}^2}{k}+E. \tag{8}$$

The effective rate of dissipation is determined to be $\hat{\varepsilon}=\varepsilon-D$, where D is added to the original model based on the low Reynolds number modifications, and the turbulent Reynolds number is defined as $R_{\mathrm{T}}=k^2/\nu\hat{\varepsilon}$. There are five empirical coefficients, which need be determined in the original k–ε two-equation model,

Table 1
Coefficients adopted by the original and a low Reynolds number k–ε turbulence models

Model	C_{μ}	$C_{\varepsilon 1}$	$C_{\varepsilon 2}$	σ_k	σ_{ε}	D	E
Original [13]	0.09	1.44	1.92	1.0	1.3	0	0
Low *Re* [14]	$0.09(1-\mathrm{e}^{-0.0115y^+})$	1.35	$1.8(1-.22\mathrm{e}^{-(R_{\mathrm{T}}/6)^2})$	1.0	1.3	$2\nu k/y^2$	$-2\nu(\tilde{\varepsilon}/y^2)\mathrm{e}^{-0.5y^+}$

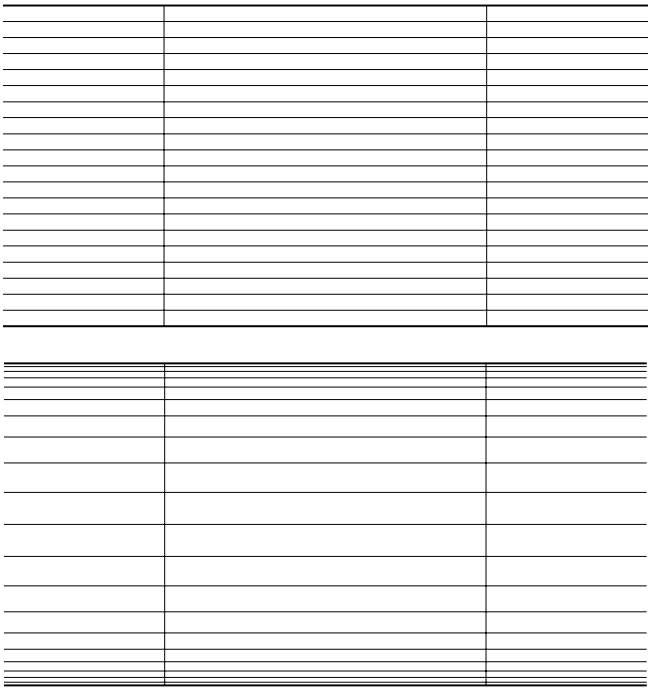

Fig. 2.The two mesh systems employed for evaluating the wall function and low Reynolds number treatments. The upper mesh is uniform in the transverse direction, and the lower mesh is non-uniform with the nearest wall cell assuming $h/dy_1 = 100$, where dy_1 is height of the first cell adjacent to the wall.

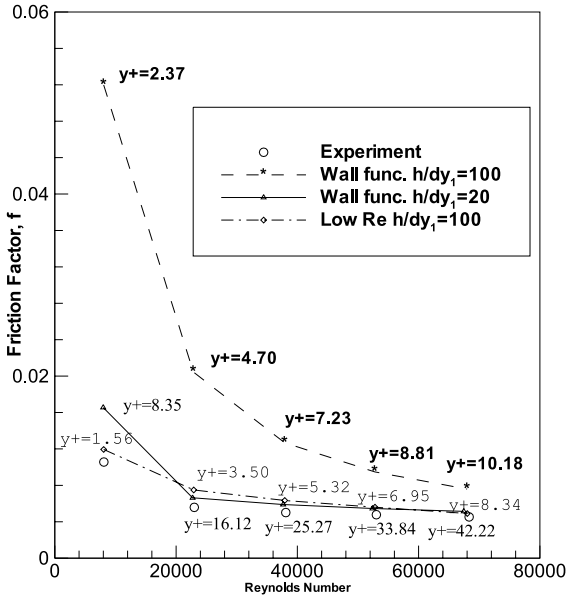

Fig. 3. Comparison of predicted and measured friction factor vs. Reynolds number for the channel flow. The y^+ values shown in the figure corresponds to the first grid point next to the solid wall (at distance dy_1 from the wall). Both wall function and low Reynolds number treatments along with two different near wall mesh distributions have been presented along with the experiment of Ha and Childs [5].

namely, the turbulent Prandtl numbers for k and ε (σ_k and σ_ε), the two coefficients regulating the magnitude of the production and dissipation in the ε equation ($C_{\varepsilon 1}$ and $C_{\varepsilon 2}$), and coefficient regulating the magnitude of the eddy viscosity (C_μ). Owing to the presence of the solid wall, the wall function treatment, as proposed in the original k–ε turbulence model, is frequently adopted in practice.

The wall function approach is based on the notion of equilibrium between production and dissipation of the turbulent kinetic energy. This scenario is valid for flows

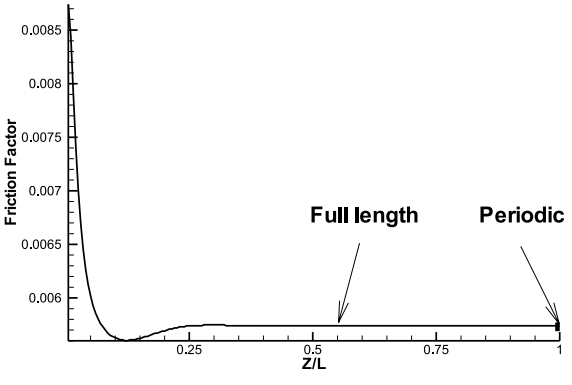

Fig. 4. Friction factor in full length and periodic seal geometry. Excellent agreement is observed between the two solutions.

Table 2
Full geometry and axially periodic boundary conditions

Full geometry BC	Periodic BC
$\overline{p}_{i=1} = 1.5\overline{p}_{i=2} - 0.5\overline{p}_{i=1}$	$\overline{p}_{i=1} = \overline{p}_{i=2} + 0.5(\overline{p}_{i=\mathrm{mid}} - \overline{p}_{i=(\mathrm{mid}+1)})$
$\bar{\rho} = \dfrac{\overline{p}}{R\tilde{T}}$	$\bar{\rho} = \dfrac{\overline{p}}{R\tilde{T}}$
$\tilde{T} = \dfrac{T_\mathrm{t}}{\left(1 + \frac{\gamma-1}{2}M^2\right)}$	$\tilde{T} = \dfrac{T_\mathrm{t}}{\left(1 + \frac{\gamma-1}{2}M^2\right)}$
$\tilde{u}_\mathrm{in} = \dfrac{\dot{m}_\mathrm{given}}{\bar{\rho}_\mathrm{in}\sum A_\mathrm{in}}$	$\tilde{u}_\mathrm{in} = \tilde{u}_\mathrm{mid}\dfrac{\dot{m}_\mathrm{given}}{\sum\left(\bar{\rho}_\mathrm{in}\tilde{u}_\mathrm{mid}A_\mathrm{in}\right)}$
$k = \dfrac{3}{2}(U_\mathrm{in}T_\mathrm{i})^2$	$k_\mathrm{in} = k_\mathrm{mid}\left(\dfrac{u_\mathrm{in}}{u_\mathrm{mid}}\right)^2$
$\varepsilon = C_\mu^{3/4}\dfrac{k^{3/2}}{l}; \quad l = 0.07h$	$\varepsilon_\mathrm{in} = \varepsilon_\mathrm{mid}\left(\dfrac{u_\mathrm{in}}{u_\mathrm{mid}}\right)^3$
$\mu_\mathrm{t} = \rho C_\mu\dfrac{k^2}{\varepsilon}$	$\mu_\mathrm{t,in} = \mu_\mathrm{t,mid}$

with no significant streamline curvatures and when $y^+ \gg 1$. If these conditions are not satisfied, a low Reynolds number modification, which resolves turbulence directly to the wall using additional damping functions D and E presented above, can be useful. The expressions for these modeling parameters are summarized in Table 1.

2.3. Assessment of the low Reynolds number model

Computations of 2-D low Reynolds number channel flows are performed to study the relative accuracy of the near-wall treatments between the wall function and low Reynolds number model. The experimental guidance is available from the test case 2 of the experimental study of Ha and Childs [5]. In their study, measurements have been made for flows between two flat plates with an inlet pressure of 12.4 bar, clearance of $h = 0.38$ mm, and length of $L = 76$ mm, making an aspect ratio of $L/h = 200$. The Reynolds number, defined based on double channel height and averaged mass flux, $Re = \rho U(2h)/\mu$, assumes the range of 8090–68,330. In

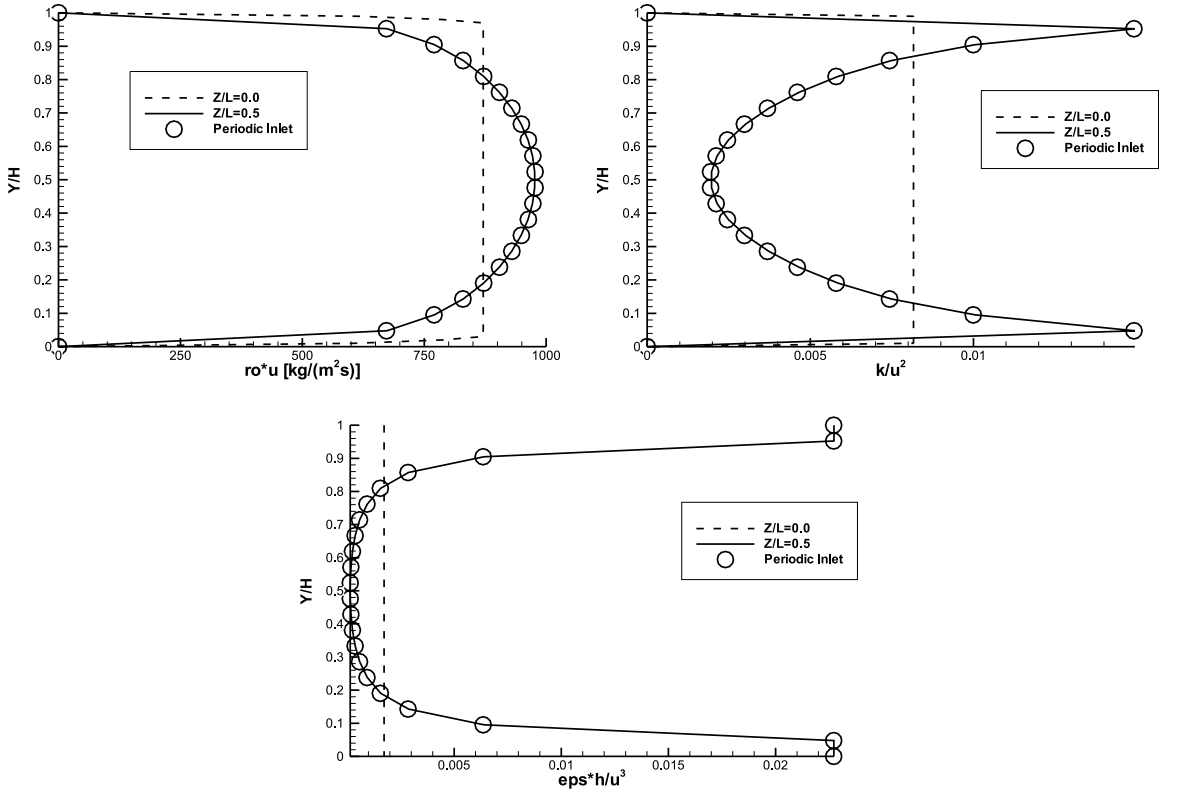

Fig. 5. Mass flux ($\overline{\rho u}$), turbulent kinetic energy ($k/\tilde{u}^2$) and eddy viscosity ($\varepsilon h/\tilde{u}^3$) profiles at the inlet of the full channel and middle of the full channel (where the flow is fully developed), and inlet values computed based on the periodic condition with 1% of the full geometry length. Excellent agreement between full and periodic treatments has been obtained.

the present computations, the domain is discretized by 201×21 nodes. The mesh is uniform along the channel length, while both uniform and non-uniform meshes in the transverse direction are considered. For non-uniform mesh, a grid-clustering law is chosen from the family of general stretching transformation discussed in [15]

$$y = h\frac{(\beta+1)[(\beta+1)/(\beta-1)]^{(2\hat{y}-1)} - \beta + 1}{2\left\{1 + [(\beta+1)/(\beta-1)]^{(2\hat{y}-1)}\right\}}, \tag{9}$$

where $\hat{y} = y/h$ is the non-dimensional distance from the wall of the channel for uniformly distributed grid. The stretching parameter β is related (approximately) to the non-dimensional boundary-layer thickness δ/h by

$$\beta = \left(1 - \frac{\delta}{h}\right)^{-1/2}, \quad 0 < \frac{\delta}{h} < 1. \tag{10}$$

Grid clustering corresponding to $\beta = 1.044$ ($h/dy_1 = 100$, where dy_1 is height of the first cell adjacent to the wall), along with a uniform mesh ($h/dy_1 = 20$) are shown in Fig. 2. Numerical solutions, with both wall functions and low Reynolds number treatments, and comparisons with the experiments are shown in Fig. 3. The results with near wall refinement show that there are significant deficiencies for the original k–ε model with the wall function treatment for such low Reynolds

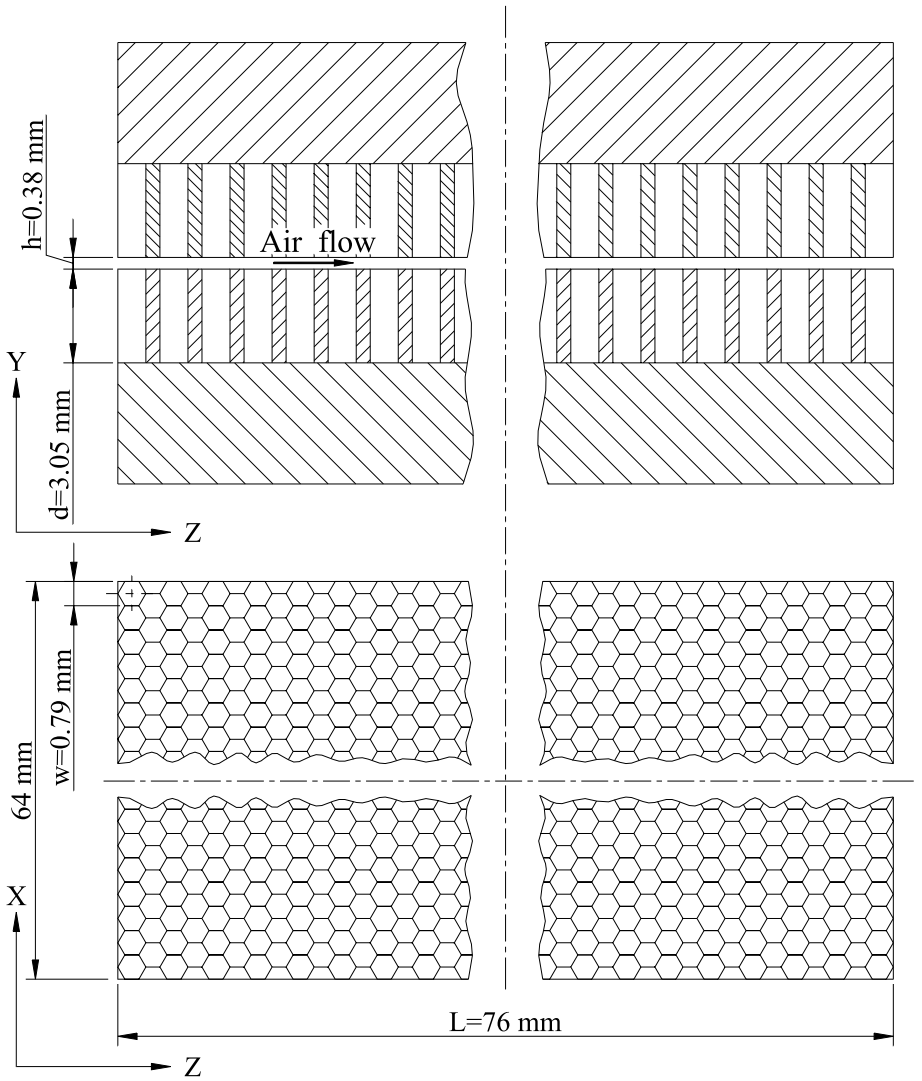

Fig. 6. Geometries of the seal with two honeycomb plates. Dimensions correspond to the test case 17 of Ha and Childs [5]. The test case 20 differs only by cell depth being 3.81 mm, in comparison with 3.05 mm in the test case 17.

number flows, because the y^+ value of the first grid point next to the solid surface becomes low and the equilibrium assumption is not valid. Uniformly distributed grid gives accurate solution only when the Reynolds number is higher then 23,000, when y^+ of the nearest wall node is more than 16. On the other hand, the low Reynolds number model with the same grid size yields reasonable solutions for the entire range of the Reynolds numbers tested. However, it is also found that the low Reynolds number model becomes computationally stiff when the overall Reynolds number becomes high. In these cases, the originally k–ε computations are conducted in the early stage of the solution procedure, with the low Reynolds number model invoked after the computation is close to reach a reasonable approximation of the flow field. It is clear from this assessment that the low Reynolds number model adopted is effective in treating the flow conditions typically encountered in honeycomb seals.

2.4. Periodic treatments for geometry with repeated patterns

For flows in long channel in a configuration with repeated geometric patterns, such as that of a honeycomb seal, it is of much interest to develop a strategy to shorten the computational domain so that more resolution can be made available to improve the numerical accuracy, and less computing time is required for obtaining a numerical solution. For example, for the present channel flow discussed, the friction factor varies when the flow structure evolves within a developing length. When the flow profile is fully developed, features such as the friction factor become unchanged. Fig. 4 shows this feature along the channel, with an aspect ratio of 200, $Re = 38,100$ and $M = 0.177$. To gain insight into the performance of a periodic treatment, a computational domain with an aspect ratio 2, or 1% of the full geometry length studied previously, is adopted for comparative evaluations. Computations for the flow in the present case, with the full channel geometry, show that the solution does not reach the fully developed condition until after passing through 30–40% of the channel length. The periodic treatment is valid only when the flow has reached a fully developed condition. For the honeycomb seals, due to geometric configurations, the flow repeats its pattern after passing through sufficient number of cells. So, even though the flow will not be fully developed, the repeatability of the flow filed warrants the adoption of the periodic treatment also. The main contributions of this work in this regard are to account for both compressibility and turbulence effects

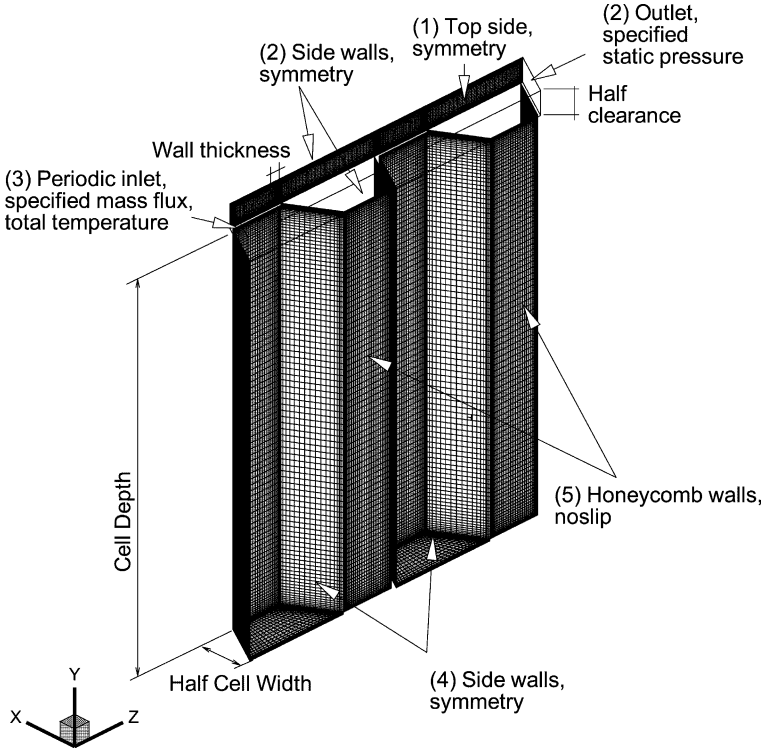

Fig. 7. The mesh system generated for the honeycomb geometry for test case 20 in the experiment of Ha and Childs [5]. In this illustration, a total of 288,192 grid points with five grid blocks are employed.

along with the velocity and pressure computations. In the following, we summarize the original development of periodic treatments for compressible, turbulent flows in geometries with repeated patterns. In the present method, the value of each dependent variable at the inlet is assigned based on that of the same variable in the middle location of the streamwise direction (subscript mid) of the periodic domain. In other words, the present treatment considers two periodic geometric elements, and chooses the midpoint value to eliminate the influence of the numerical outlet treatment. The values known a priori in both full and periodic geometries are the mass flow rate, $\dot{m}$, and the total inlet temperature, T_t. Of course, for an adiabatic wall condition, which is the case in the present study, the total temperature remains unchanged in the entire flow domain.

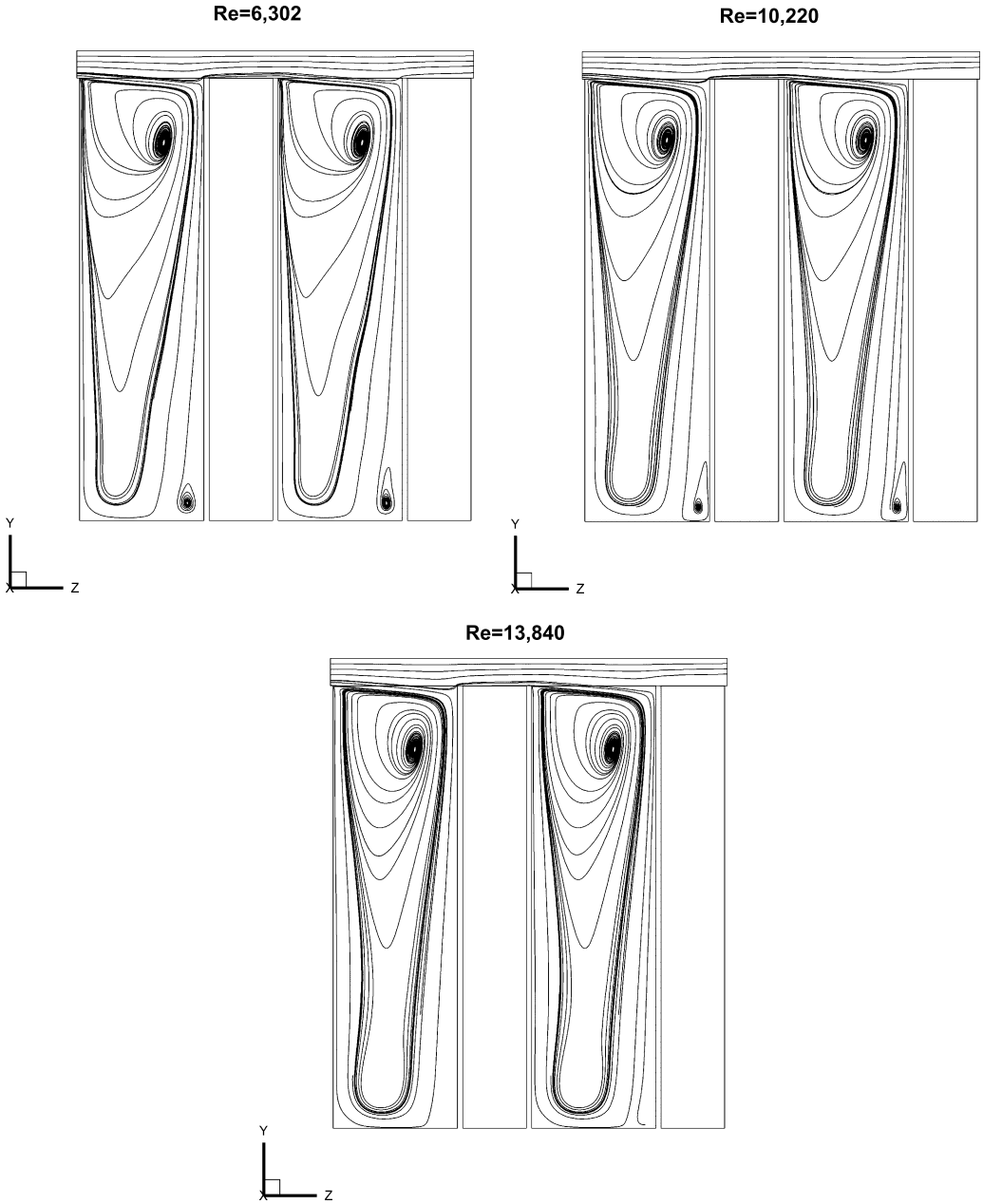

Fig. 8. Streamline plots, in the symmetry plane of the honeycomb cell, for the test case 17 of Ha and Childs [5]. Cell width = 0.79 mm, cell depth = 3.05 mm, clearance = 0.38 mm. Inlet pressure is 6.9 bar.

Specific formulas proposed for the periodic boundary conditions for the compressible, turbulent flow are shown in Table 2. The inlet pressure for the standard BC with no periodic consideration is extrapolated from the two near-inlet points. For the periodic inlet, the near-inlet values are extrapolated from the near-inlet value using pressure gradient developed at the middle of the domain, along the streamwise di-

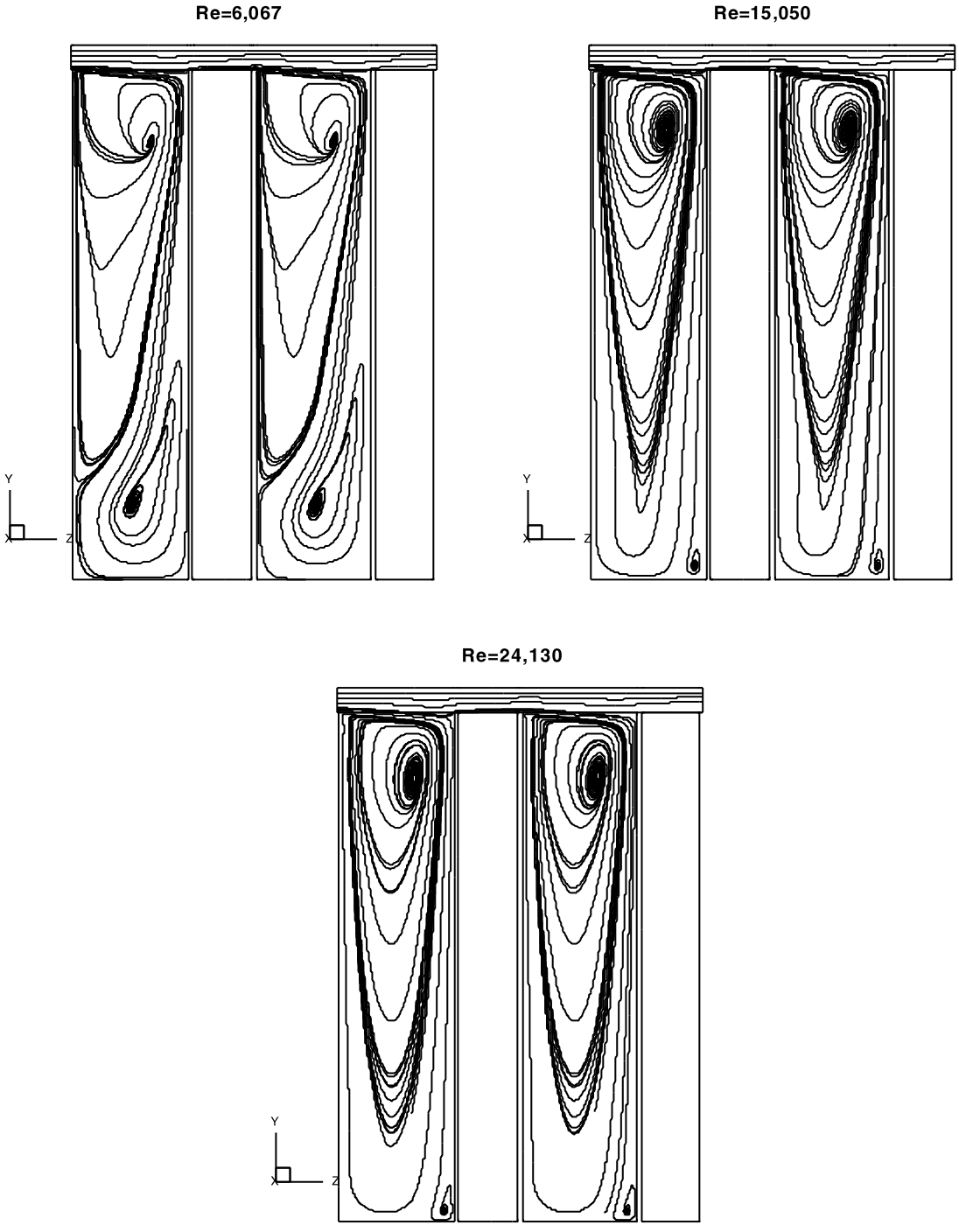

Fig. 9. Streamline plots, in the symmetry plane of the honeycomb cell, for the test case 20 of Ha and Childs [5]. Cell width = 0.79 mm, cell depth = 3.05 mm, clearance = 0.38 mm. Inlet pressure is 6.9 bar.

rection. Density in both full and periodic geometries is obtained from the equation of state, and the inlet temperature is calculated from the total temperature and the local Mach number. Inlet velocities in the full geometry treatment are found based on the given mass flow rate and local density. In the periodic treatment, the velocity profile from the middle of the domain is adopted in the inlet with a scaling procedure. The scaling procedure is to account for the fact that the temperature and pressure, and hence the density values at the inlet and the midpoint are different. To ensure that the mass conservation is satisfied, a simple linear scaling is devised. This aspect makes the current treatment different from those periodic treatments for incompressible, constant property flows. Furthermore, the inlet turbulence quantities for the periodic treatment also need to be scaled based on the dimensional laws of the individual variables [16], as shown in Table 2. Specifically, in the present periodic treatment, the inlet k and ε profiles are copied from the corresponding variables in the middle of the domain, and scaled based on the absolute velocity ratio in power 2 and 3, respectively.

Fig. 5 demonstrates the validity of the proposed periodic treatment by plotting mass flux and non-dimensionalized turbulence kinetic energy and eddy dissipation rate. As the flow in the channel becomes fully developed, the profiles of these variables become unchanged and serve as the basis for periodic boundary conditions.

3. Results and discussions

3.1. Experimental setup of the honeycomb seals

In addition to the smooth geometries, Ha and Childs [5] have experimentally studied flows between two

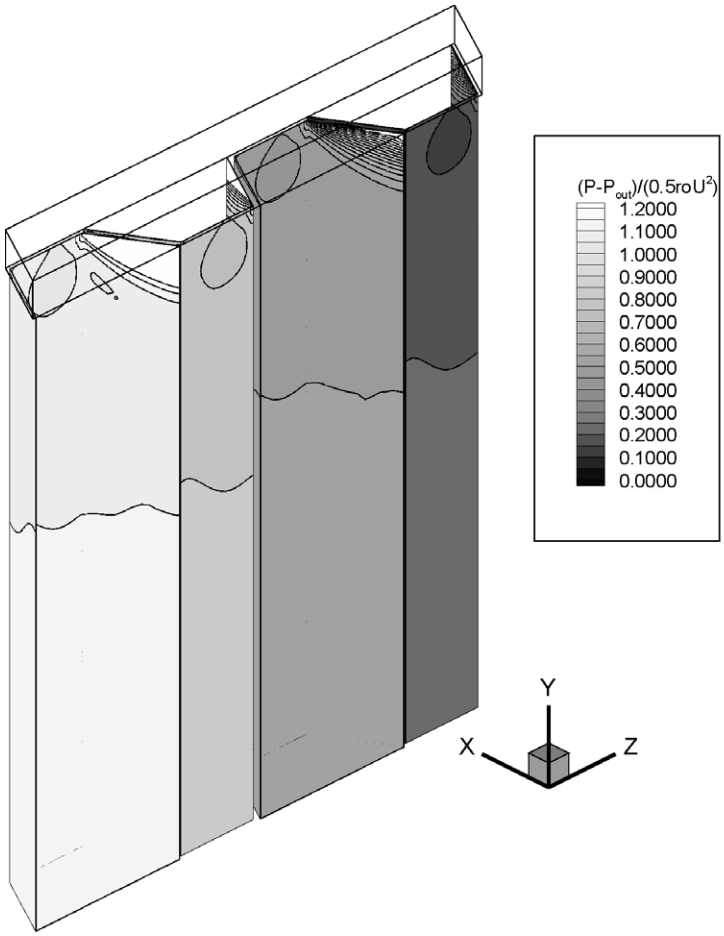

Fig. 10. Representative pressure contours on the cell walls, $f_p = 0.077$. Cell depth 3.05 mm, $Re = 6302$. For related information, see Fig. 8.

honeycomb plates, placed against each other with a small gap between them. Fig. 6 shows the geometrical characteristics of the test case 17. The test case 20 differs only in the cell depth, which is 3.81 mm, in comparison of 3.05 mm in the test case 17. In both cases, the clearance between the two honeycomb plates is 0.38 mm, the inlet pressure is 6.9 bar. The Reynolds number ranges from 6067 to 24,130 and the Mach number range is 0.045–0.235. The friction factor measured by them varies from 0.03185 to 0.13594 and is significantly higher in their test case 17.

Reynolds and Mach numbers affect the thermo-fluid-dynamics parameters. In the present study, the effect of Mach number is largely reflected in the variations in pressure, temperature and density profiles. Consequently, the Mach number affects the detailed periodic treatment. Its impact on parameters such as the loss mechanisms is insignificant for low subsonic flows, as is the case here. The experimental studies [5] show that the measured losses for various honeycomb geometries are not only sensitive to small changes in geometric variations, but in general do not correlate well with the Reynolds number. Noticeably, the so-called friction-factor-jump phenomenon is observed, which results from the unsteady interaction between forced acoustic response of the flow around cells and the amplification of feedback disturbances of the mainstream flow. Such a behavior is similar to that observed in flows over a cavity [17,18] involving strong acoustic radiation. In the present study, we will not address issues related to friction-factor-jumps, and focus on the steady-state formulation to gain insight into the fundamental physics and numerics associated with such geometries and operating parameters.

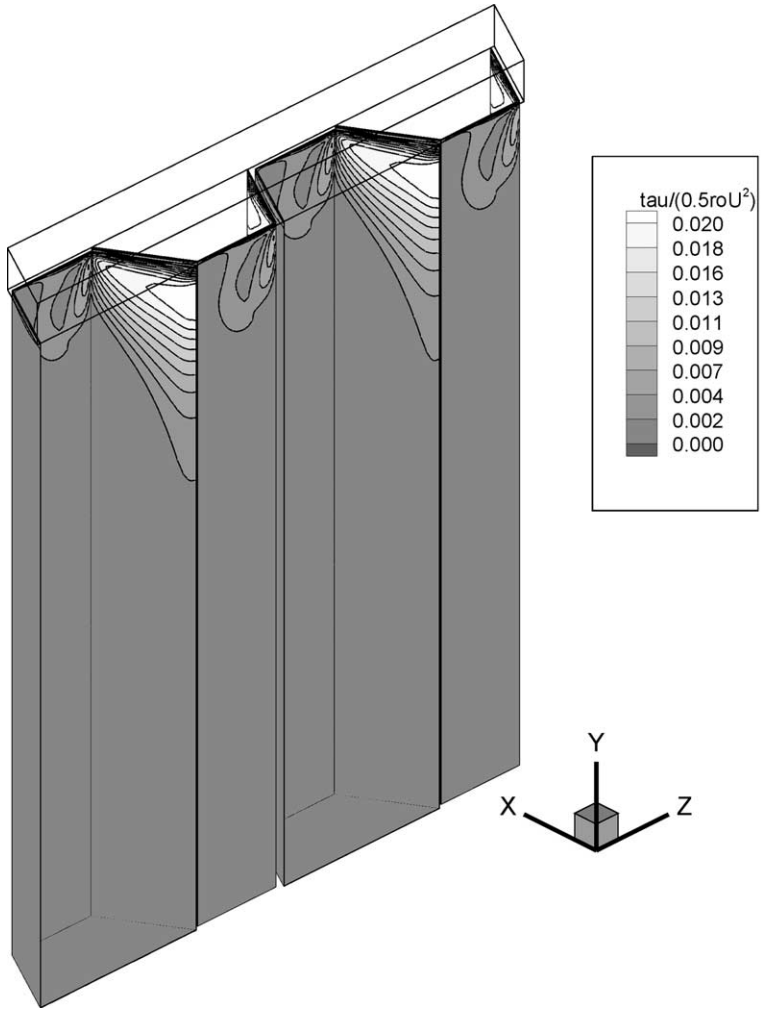

Fig. 11. Contours of near-wall shear stress absolute values at the cell walls, $f_\tau = 0.005$. Cell depth 3.05 mm, $Re = 6302$. For related information, see Fig. 8.

3.2. Computational results

As already established, the operational conditions of the honeycomb seals require a low Reynolds number turbulence model. In order to employ such a model, a dense mesh is needed in the wall region in order to obtain near-wall $y^+ < 5$. A representative view of the mesh system generated is offered in Fig. 7. Only half of the domain is considered in the direction of the clearance, modeled by the symmetry boundary condition. Since there is no transverse wall motion, symmetry boundary conditions are used in the transverse (X) direction, shown as sides 2 and 4 in the figure. Periodic inlet and outlet conditions developed in this work are considered in the streamwise direction (Z). It should be emphasized that the honeycomb walls have finite thickness, which is accounted for in order to provide desirable level of numerical fidelity.

Figs. 8 and 9 depict streamlines in the symmetry plane with the honeycomb cells shown in Fig. 7, for test cases 17 and 20, respectively. In each figure, results with different Reynolds numbers are depicted. In general, one observes two contra-rotating vortices in each cell. The higher the Reynolds number, the more volume the primary vortex occupies. After certain Reynolds numbers, the primary cell reaches the bottom of the cell, and further increasing Re does not affect the qualitative flow pattern.

3.3. Loss mechanisms

When analyzing the total friction factor, one simply performs integration to obtain the total pressure at the inlet and outlet, and computes the loss based on the difference between them, i.e.,

$$f = \frac{\int_{\text{inlet}}(-p_t)n_3\,\mathrm{d}A - \int_{\text{outlet}}(-p_t)n_3\,\mathrm{d}A}{0.5\rho U^2 A_{\text{w}}}, \tag{11}$$

where A cross-sectional area of the inlet/outlet, A_{w} is the effective area of the plate surfaces, $0.5\rho U^2$ is the averaged dynamic pressure, and n_3 is direction cosine between the inlet/outlet normal and the flow (Z) direction. Of course, there are different physical mechanisms responsible for the loss, one being the shear stress at the solid wall, the other being the pressure-induced loss due to the change in the effective geometry of the honeycomb seal, due to the viscous effect. The pressure-induced loss results from the mixing process between fluid particles inside the cell. In order to gain insight into the relative contributions between wall shear stress and pressure-induced loss, we plot pressure and wall shear

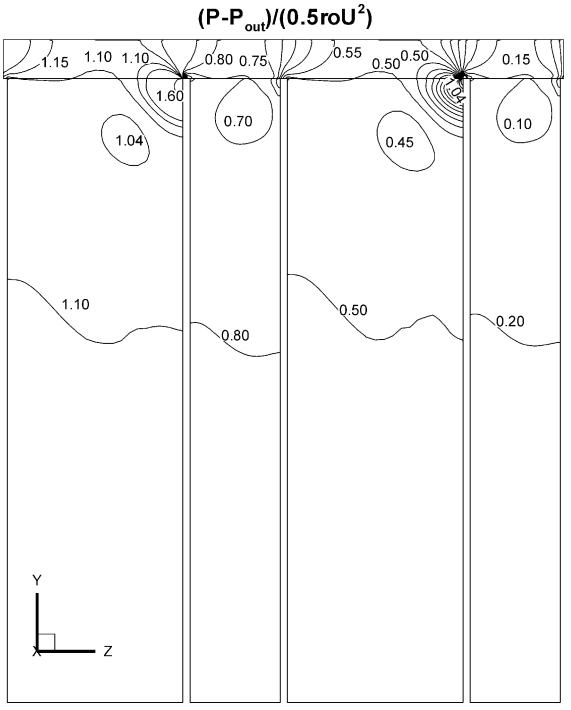

Fig. 12. Pressure contours in Y–Z plane through the plane of symmetry. Flow is from left to right. Cell depth 3.05 mm, $Re = 6302$. For related information, see Fig. 8.

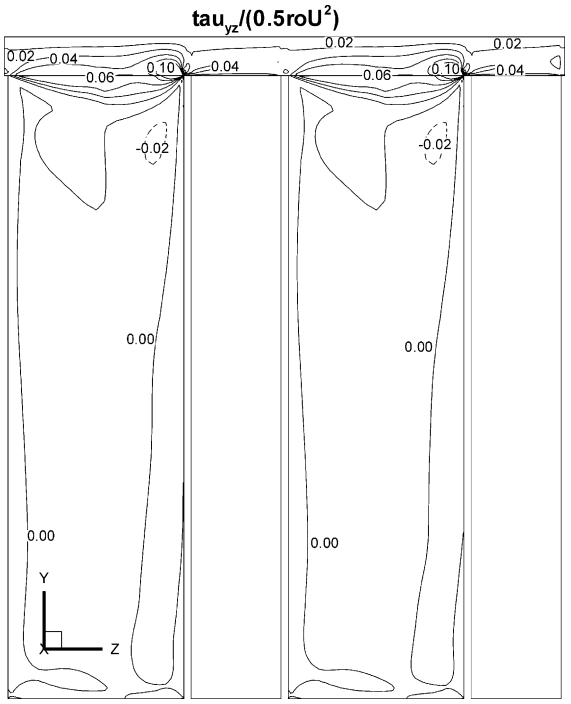

Fig. 13. Wall shear stress $\tau_{yz}/0.5\rho U^2$ contours in Y–Z plane through the plane of symmetry. Flow is from left to right. Cell depth 3.05 mm, $Re = 6302$. For related information, see Fig. 8.

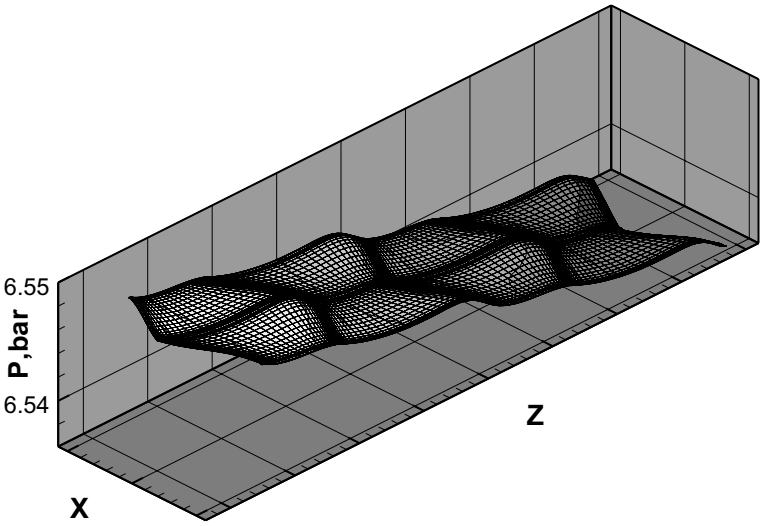

Fig. 14. Typical pressure plot at the middle plane between two honeycomb plates. Flow is in positive Z direction. Periodic domain with four cells is shown twice, using advantage of sidewise symmetry. For related information, see Fig. 8.

stress contours, respectively, on the honeycomb walls in Figs. 10 and 11. Integration in the flow direction (Z) yields

$$f_{\mathrm{p}} = \frac{\int_{\mathrm{walls}}(-p)n_3\,\mathrm{d}A}{0.5\rho U^2 A_{\mathrm{w}}} = 0.077, \tag{12}$$

$$f_{\tau} = \frac{\int_{\mathrm{walls}}\tau_{\mathrm{wall}}t_3\,\mathrm{d}A}{0.5\rho U^2 A_{\mathrm{w}}} = 0.005, \tag{13}$$

where τ_{wall} is wall shear stress at honeycomb walls and t_3 is directional cosine between wall shear stress vector and flow (Z) direction. Hence the pressure drag is 15.4 times

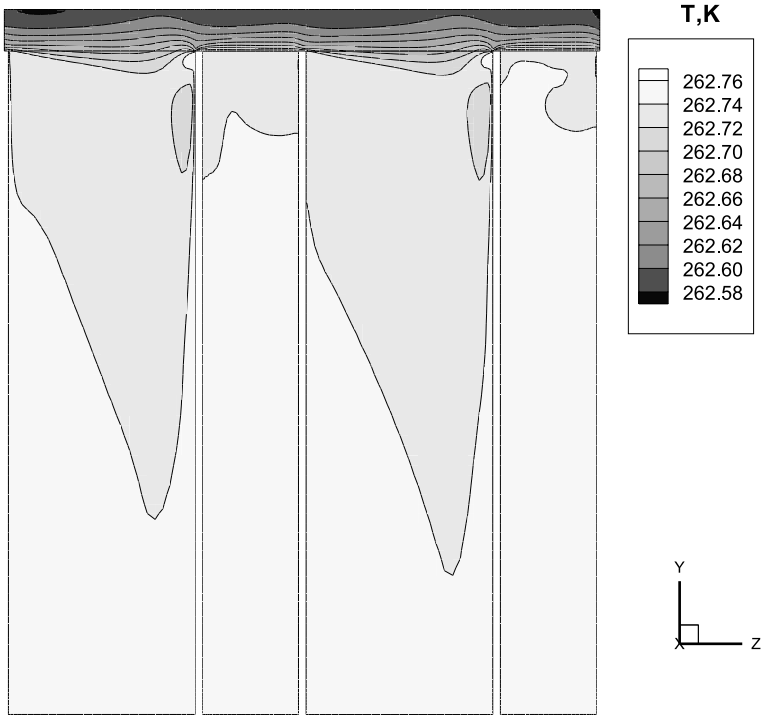

Fig. 15. Temperature contours in Y–Z plane through the plane of symmetry. Flow is from left to right. Cell depth 3.05 mm, $Re = 6302$. For related information, see Fig. 8.

higher than friction drag in the honeycomb seal. This observation can help explain why honeycomb seals can better control the leakage in comparison to smooth seals. The pressure drag production mechanism can be seen in Figs. 12 and 13. Strong recirculation at the neck of the cell produces shear stress gradients, which is balanced in part by the pressure gradients.

Fig. 14 shows pressure plots resulted at the middle plane between the plates. It presents characteristic steps in which pressure decreasing from an upstream cell to a downstream cell. High mesh density, required by low Reynolds number models, is helpful in capturing sharp gradients between cells.

Fig. 15 shows temperature contours associated with the flow field around the honeycomb cells. The Mach number for the case shown is low, 0.049. The temperature gradually increases in the clearance direction from the centerline to the cell bottom. For higher Mach number flows in the range considered, the temperature level increases faster with similar qualitative characteristics.

4. Conclusions

Steady-state numerical computations employing a low Reynolds number turbulence model are compared with experimental results for flow between two straight honeycomb plates. Periodic boundary conditions for compressible, turbulent flow with pressure gradient are developed allowing computational consideration of smaller portion of the physical domain with improved resolution. Even though the Mach number is low, the compressibility effect influences the development of the thermal variables, and hence the periodic boundary conditions. Turbulence modeling has a strong effect on the present flow regime. In the context of the k–ε two-equation model, it is shown that the low Reynolds number model performs better than the wall function treatment.

The computations show that as Re is increased, the primary vortex penetrates deeper toward the bottom of the honeycomb cell. On the other hand, the friction-factor-jump phenomenon is observed experimentally but not by steady-state computations. For honeycomb seals, the pressure drag (form drag) dominates the wall shear stress. Strong pressure gradients in vicinity of the downstream walls are balanced by enhanced shear stresses from the mixing process. This observation helps explain why honeycomb seals can better control flow leakage compared to the smooth wall seals.

Acknowledgements

The present research has been supported in part by Dresser-Rand Co.

References

[1] J. Scharrer, Discussion in paper, annular honeycomb seals: test results for leakage and rotordynamic coefficients; comparisons to labyrinth and smooth configurations, by Childs et al., ASME J. Tribol. 111 (1989) 300–301.

[2] D. Childs, D. Elrod, K. Hale, Annular honeycomb seals: test results for leakage and rotordynamic coefficients; comparisons to labyrinth and smooth configurations, ASME J. Tribol. 111 (1989) 293–300.

[3] G. Kleynhans, A comparison of experimental results and theoretical predictions for the rotordynamic and leakage characteristics of short $(L/D = 1/6)$ honeycomb and smooth annular pressure seals, TRC-SEAL-12-91 #346, Turbomachinery Laboratory Report, Texas A&M University, December 1991.

[4] G. Hirs, A bulk-flow theory for turbulence in lubricating films, ASME J. Lubr. Technol. (April) (1973) 137–146.

[5] T.W. Ha, D.W. Childs, Friction-factor data for flat plate tests of smooth and honeycomb surfaces (including extended test data), TL-SEAL-1-91 #343, Turbomachinery Laboratory Report, Texas A&M University, January 1991.

[6] T.W. Ha, Rotordynamic analysis of annular honeycomb-stator turbulent gas seals using a new friction factor model based on flat plate tests, Ph.D. Thesis, Texas A&M University, College Station, TX, 1992.

[7] T.W. Ha, D.W. Childs, Annular honeycomb-stator turbulent gas seal analysis using new friction-factor model based on flat plate tests, ASME J. Tribol. 116 (1994) 352–360.

[8] R.C. Hendricks, B.M. Steinetz, M.M. Athavale, A.J. Przekwas, Seals/Secondary Flows, Selected NASA LeRC Results with Emphasis on CFD, NASA Seals/Secondary Flows Workshop, CP 10198, October 23–24, Cleveland, OH, 1997.

[9] S. Thakur, W. Shyy, Some implementational issues of convection schemes for finite-volume formulations, Numer. Heat Transfer B 24 (1993) 31–55.

[10] W. Shyy, Computational Modeling for Fluid Flow and Interfacial Transport, Elsevier, Amsterdam, 1994 (Chapter 5).

[11] W. Shyy, S.S. Thakur, H. Ouyang, J. Liu, E. Blosch, Computational Techniques for Complex Transport Phenomena, Cambridge University Press, Cambridge, 1997 (Chapter 2).

[12] J. Wright, W. Shyy, A pressure-based composite grid method for the Navier–Stokes equations, J. Comput. Phys. 107 (1993) 225–238.

[13] B.E. Launder, D.B. Spalding, The numerical computation of turbulent flows, Comput. Meth. Appl. Mech. Eng. 3 (1974) 269–289.

[14] K. Chien, Predictions of channel and boundary-layer flows with a low-Reynolds-number turbulence model, AIAA J. 20 (1982) 33–38.

[15] J.C. Tannehill, D.A. Anderson, R.H. Pletcher, in: Computational Fluid Mechanics and Heat Transfer, second ed., Taylor & Francis, London, 1997, pp. 333–336.

[16] H.K. Versteeg, W. Malalasekera, in: An Introduction to Computational Fluid Dynamics. The Finite Volume Method, Longman, New York, 1995, pp. 72–75.

[17] D. Rockwell, E. Naudascher, Review – self-sustaining oscillations of flow past cavities, ASME J. Fluid Eng. 100 (1978) 152–165.

[18] L.N. Cattafesta III, S. Garg, M. Choudhari, F. Li, Active control of flow-induced cavity resonance, AIAA Paper 97-1804, 1997.